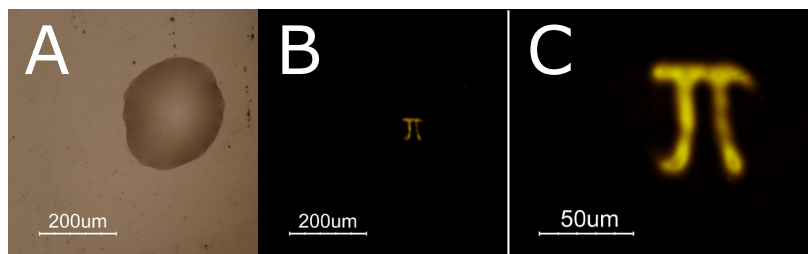


Fluorescent microstructure fabrication



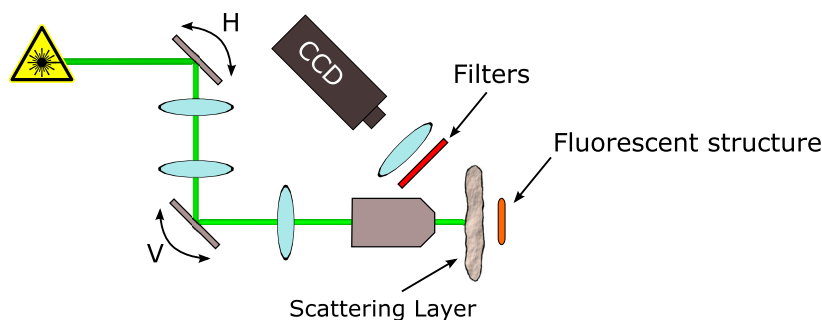
Supplementary Figure 1 : (a) White light microscope image of the bleached dye-doped polymer droplet. Since all the dye was bleached the droplet appears transparent. The unbleached π -shaped area is faintly visible in pink on the lower-left quarter of the droplet. (b) Same image as in panel a but illuminating the droplet with green light and collecting only the fluorescence using a band-pass filter. The shape of the fluorescent pattern is now clearly visible against the black background. (c) Same as in panel b but with a higher magnification. The image appears slightly out of focus because the structure thickness (determined by the droplet thickness) is larger than the focal depth of the microscope objective used.

To fabricate the fluorescent microstructures we mixed 2 mg of Rhodamine 6G dye powder with 1 ml of an UV-curable acrylate monomer (Norlan optical adhesive 65). Placing the mixture on the roller bank for half an hour and in the ultrasonic bath for 15 minutes produced a homogeneous solution without any residual grain of dye. A small droplet of the solution was then deposited on a 1 mm thick glass cover slide with the aid of a pin. We found that drops of $\sim 200\mu\text{m}$ diameter could be made in a consistent and reproducible way. The glass slide was then placed under a UV lamp for 10 minutes to cure the polymer, thus making the droplet solid.

Successively the dye-doped polymer was illuminated with the 466 nm line of an Argon laser. The intensity profile of the beam was shaped using a micromirror device³¹. The part of the droplet illuminated by the laser beam irreversibly bleached, gradually losing its ability to fluoresce. On the other side the areas that, due to the amplitude modulation, were not illuminated were not damaged and remained fluorescent. We continuously monitored the fluorescence from the droplet with a CCD camera and stopped the bleaching process when no signal was detected anymore, signifying that all the dye in the illuminated area was completely bleached. This process typically took about 40 minutes. Supplementary Figure 1 shows a white light microscope image of the bleached droplet (panel a), the same droplet but looking at the fluorescence (panel b) and a magnification of the fluorescent structure (panel c).

This procedure allows to fabricate fluorescent 2D structures with arbitrarily complex shape and with a resolution better than $10\mu\text{m}$ in a simple and reproducible way.

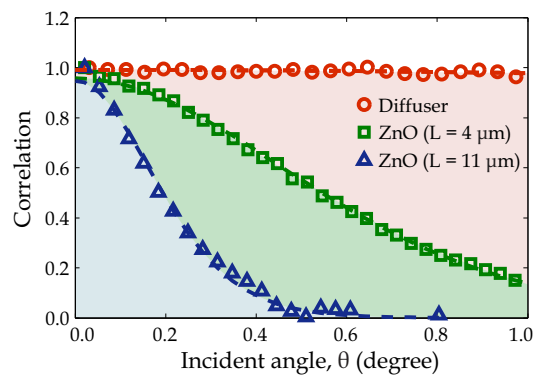
Measurement setup



Supplementary Figure 2 : Schematic of the setup used for the measurements. Folding mirrors, polarizers and neutral density filters are not shown here.

As shown in Supplementary Figure 2, the light coming from a solid-state laser ($\lambda = 532 \text{ nm}$) is incident on a mirror (a GVS011 galvanic mirror from Thorlabs) that can rotate around the vertical axis. This first mirror is imaged on a second galvanic mirror, rotating around the horizontal axis, via 2 relay lenses with focal length $f = 100 \text{ mm}$, in a $4f$ configuration. The second mirror is then demagnified and imaged on the surface of the scattering layer via a tube lens ($f = 100 \text{ mm}$) and a 10x Nikon microscope objective ($\text{NA}=0.25$). Using this configuration we can freely rotate the angle of incidence of the laser light on the scattering surface without changing the incident position. To detect the signal from the front side we used a combination of a Notch filter (Semrock NF01-532U-25) and a band-pass filter (Semrock FF01-593/40-25) to separate the excitation light from the fluorescence. The fluorescent intensity on the surface of the scattering medium was then imaged on a CCD (a Dolphin camera from Allied Vision Technology).

The speckle memory effect



Supplementary Figure 3 : Comparison between the measured correlation for the memory effect and the theoretical curves.

Coherent light is scrambled by disorder. As a result a collimated beam of light transmitted through a scattering material emerge as a collection of bright and dark spots known as speckle. Despite its apparent randomness laser speckle retains some information on both the incident beam the the scattering material in the form of correlations. One of the most apparent manifestations of this phenomenon is the fact, named *memory effect*, that changing the angle of incidence of the light on a scattering slab by an angle $\Delta\theta$ does not change completely the resulting speckle pattern. For small angles the speckle pattern is essentially unchanged but only rotated by the same angle $\Delta\theta$. For larger angles the speckle pattern is modified gradually and its correlation with the one for $\Delta\theta = 0$ decay continuously as

$$C(|\Delta\theta|) = (k|\Delta\theta|L / \sinh(k|\Delta\theta|L))^2, \quad (1)$$

where L is the scattering layer thickness and k is the wave vector³²⁻³⁴. Notice that this correlation is independent from the scattering strength of the material.

We measured $C(|\Delta\theta|)$ for the diffuser used in the experiment and for two scattering layer made by spray-painting ZnO particles with an average diameter of 200 nm on a microscope cover slide³⁵ with thicknesses L equal to, respectively, $4\mu\text{m}$ and $11\mu\text{m}$. In Supplementary Figure 3 the experimental data are compared with the theoretical curve (eq. 1). Ground glass optical diffusers are completely opaque but, at the same time, very thin. Therefore $C(|\Delta\theta|) \simeq 1$ for all angles used in the experiment.

Windowing of the autocorrelation

When we compute the autocorrelation from the measured $I = O * S$ we have to take into consideration that we can only probe a limited range of Δr . We found that, if the autocorrelation is calculated directly as $I \star I$, the image retrieval algorithm described below always produced hot spots in the reconstructed picture. To avoid these artifacts we first windowed I with a Hamming window w and then computed the autocorrelation as

$$I \star I = \frac{[(O * S) \cdot w] \star [(O * S) \cdot w]}{w \cdot w}. \quad (2)$$

To suppress the inevitable increase in noise at the edges of the picture we windowed the autocorrelation with a Tukey window³⁶.

Convergence of the speckle autocorrelation

The success of our method depends on the signal to noise ratio of the measured autocorrelation. The main contribution to the noise is the residual speckle, which depends on the solid angle scanned. In fact we assume the averaged autocorrelation of the speckle $\langle S \star S \rangle$ to have the form of an Airy disk, but this is rigorously true only if the average includes an infinitely large amount of speckle spots. If the scanned solid angle is finite only a limited number of speckle spots will contribute to the average and this will reduce the signal to noise ratio. We have numerically checked that the signal to noise is proportional to the square root of the number of speckle spots included in the scanned range. To obtain good signal to noise one could make one large scan or several non-overlapping smaller scans. We find it is experimentally more convenient, in view of long scan times, to make a number of non-overlapping scans and average their autocorrelates. Similar results are obtained if adjacent scans are patched together before computing the autocorrelate.

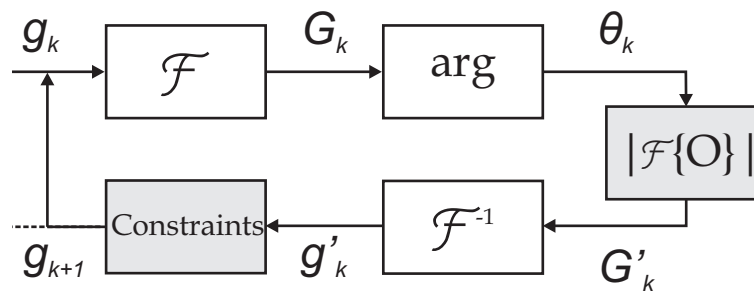
Image retrieval

In general it is impossible to recover an object from its autocorrelate since the calculation of an autocorrelation is a lossy operation. An autocorrelate preserves only the magnitude of the spatial Fourier spectrum while all phase information is lost. This loss is seen by calculating the Fourier transform of an autocorrelation using the convolution theorem

$$\mathcal{F}\{O \star O\} = \mathcal{F}\{O\}\mathcal{F}\{O\}^* = |\mathcal{F}\{O\}|^2. \tag{3}$$

In practice however, it is often possible to uniquely infer the lost phase information for objects that have a dimensionality higher than one³⁷⁻³⁹. Fienup^{40,41} pioneered such methods for phase retrieval and demonstrated several iterative algorithms that are capable of retrieving an object from the magnitude of the spatial Fourier spectrum by using a priori information of the object, such as being real or non-negative. These algorithms were quickly adopted in a wide variety of fields, such as astronomy and crystallography^{42,43}.

Phase retrieval algorithms



Supplementary Figure 4 : Block diagram for an iterative phase recovery algorithm. \mathcal{F} : Fourier transform; Arg: argument; $|\mathcal{F}\{O\}|$ Magnitude of the measured spatial spectrum of the object O ; which is retrieved from the autocorrelation of O . inverse Fourier transform; \mathcal{F}^{-1} inverse Fourier transform; Constraints: real space constraints to calculate g_{k+1} out of g_k .

The basics of Fienup’s phase retrieval algorithms are shown in Supplementary Figure 4 . The algorithm starts with an initial guess $g_1(x, y)$ of the object. When a low resolution image of the object is available, this image is a logical

choice for the initial guess. Otherwise, a completely random pattern can be used to start the algorithm. The initial guess is entered into an algorithm that performs the following four steps at its k^{th} iteration

$$\begin{aligned} G_k(u, v) &= \mathcal{F}\{g_k(x, y)\} \\ \theta_k(u, v) &= \arg G_k(u, v) \\ G'_k(u, v) &= |\mathcal{F}\{O(x, y)\}|e^{i\theta_k(u, v)} \\ g'_k(x, y) &= \mathcal{F}^{-1}\{G'_k(u, v)\}, \end{aligned} \quad (4)$$

where we use the information from the measured autocorrelation in the third step.

At this point the algorithm requires real space constraints on the object. In our case, where we look at the amount of fluorescence coming from the object, O has to be real and positive. We define a set Γ that contains all the points in g'_k violating this constraint; in our case the points with a negative or complex value. There are multiple ways to implement this constraint into the algorithm. The first implementation is known as the 'Error-Reduction' algorithm and sets

$$g_{k+1}(x, y) = \begin{cases} g'_k(x, y) & \text{for } (x, y) \notin \Gamma \\ 0 & \text{for } (x, y) \in \Gamma \end{cases}. \quad (5)$$

Another possible implementation is called the 'Hybrid Input-Output' algorithm and defines

$$g_{k+1}(x, y) = \begin{cases} g'_k(x, y) & \text{for } (x, y) \notin \Gamma \\ g_k(x, y) - \beta g'_k(x, y) & \text{for } (x, y) \in \Gamma \end{cases}, \quad (6)$$

where β is a feedback parameter that control the convergence properties of the algorithm⁴¹. When $g_{k+1}(x, y)$ is calculated it can be used as the starting point for the $(k + 1)^{\text{th}}$ iteration. A single iteration of these algorithms takes only a couple of microseconds on a modern desktop computer allowing for a complete inversion of an autocorrelation within a few seconds.

The convergence of the algorithms is monitored by calculating the squared error E_k^2 between the autocorrelation of the retrieved image with the measured one

$$E_k^2 = (|\mathcal{F}\{g'_k\}| - |\mathcal{F}\{O\}|)^2. \quad (7)$$

Consistently with the scheme already suggested in⁴¹, we found the best convergence by starting with the Hybrid Input-Output algorithm and gradually lowering β from 2 to 0 in steps of 0.05 and running 10 iteration per value of β . Then we run 100 iterations with the Error-Reduction algorithm to reduce any residual noise from the image.

-
- [31] Akbulut, D., Huisman, T. J., van Putten, E. G., Vos, W. L. & Mosk, A. P. Focusing light through random photonic media by binary amplitude modulation. *Opt. Expr.* **19**, 4017–4029 (2011).
- [32] Feng, S., Kane, C., Lee, P. A. & Stone, A. D. Correlations and fluctuations of coherent wave transmission through disordered media. *Phys. Rev. Lett.* **61**, 834–837 (1988).
- [33] Freund, I., Rosenbluh, M. & Feng, S. Memory effects in propagation of optical waves through disordered media. *Phys. Rev. Lett.* **61**, 2328–2331 (1988).
- [34] Akkermans, E. & Montambaux, G. *Mesoscopic Physics of Electrons and Photons* (Cambridge University Press, 2007).
- [35] Vellekoop, I. M. & Mosk, A. P. Universal optimal transmission of light through disordered materials. *Phys. Rev. Lett.* **101** (2008).
- [36] Press, W. H., Teukolsky, S. A., Vetterling, W. T. & Flannery, B. P. *Numerical Recipes 3rd Edition: The Art of Scientific Computing* (Cambridge University Press, 2007).
- [37] Bates, R. H. T. Fourier phase problems are uniquely solvable in more than one dimension. i: underlying theory. *Optik* **61**, 247–262 (1982).
- [38] Bates, R. H. T. Uniqueness of solutions to two-dimensional fourier phase problems for localized and positive images. *Computer Vision, Graphics, and Image Processing* **25**, 205 – 217 (1984).
- [39] Barakat, R. & Newsam, G. Necessary conditions for a unique solution to two-dimensional phase recovery. *Journal of Mathematical Physics* **25**, 3190–3193 (1984).
- [40] Fienup, J. R. Reconstruction of an object from the modulus of its fourier transform. *Opt. Lett.* **3**, 27–29 (1978).
- [41] Fienup, J. R. Phase retrieval algorithms: a comparison. *Appl. Opt.* **21**, 2758–2769 (1982).
- [42] Miao, J., Charalambous, P., Kirz, J. & Sayre, D. Extending the methodology of x-ray crystallography to allow imaging of micrometre-sized non-crystalline specimens. *Nature* **400**, 342–344 (1999).
- [43] Abbey, B. *et al.* Lensless imaging using broadband x-ray sources. *Nat. Photon.* **5**, 420–424 (2011).